The Heat Balance of the Western Hemisphere Warm Pool

David B. Enfield[1] and Sang-ki Lee[2]

[1] NOAA Atlantic Oceanographic and Meteorological Laboratory, Miami, FL, 33149
[2] Cooperative Institute for Marine & Atmospheric Studies

Submitted to *Journal of Climate*

February 2004

Abstract.

We have analyzed the thermodynamic development of the Western Hemisphere warm pool and its four geographic subregions. The subregional warm pools of the eastern North Pacific and equatorial Atlantic are best developed in the boreal spring, while in the Gulf of Mexico and Caribbean the highest temperatures prevail during the early and late summer, respectively. For the defining isotherms chosen (≥27.5°C, ≥28.0°C, ≥28.5°C) the warm pool depths are similar to the mixed layer depth (20-40 m) but considerably less than the Indo-Pacific warm pool depth (50-60 m). The heat balance of the WHWP subregions is examined through two successive types of analysis, first by considering a changing volume ("bubble") bounded by constant temperature wherein advective fluxes disappear and diffusive fluxes can be estimated as a residual; second by considering a slab layer of constant dimensions with the bubble diffusion estimates as an additional input and the advective heat flux divergence as a residual output. From this sequential procedure it is possible to disqualify as being physically inconsistent, four of seven surface heat flux climatologies: the NCEP and ERA15 reanalyses because they yield a non-physical diffusion of heat into the warm pools from their cooler surroundings; and the unconstrained da Silva and Southampton data sets because their estimated diffusion rates are inconsistent with the smaller rates of the better understood Indo-Pacific warm pool when the bubble analysis is applied to both regions. The remaining surface flux data sets of da Silva and Southampton (constrained) and Oberhuber have a much narrower range of slab surface warming (+25 ±5 W/m^2) associated with bubble residual estimates of total diffusion of –5 to –20 W/m^2 (±5 W/m^2) and total advective heat flux divergence of –2 to –14 W/m^2 (±5 W/m^2). The latter are independently confirmed by direct estimates using wind stress data and drifters for the Gulf of Mexico and eastern North Pacific subregions. Heat balance studies of warm tropical ocean regions are found to be better-served by the globally constrained surface fluxes of da Silva and Southampton rather than the unconstrained data sets or the reanalyses.

1. Introduction

Unlike the Indo-Pacific warm pool, the Western Hemisphere warm pool (WHWP, Weisberg 1996) undergoes a very large annual variation in its geographic extent, almost disappearing in the boreal winter while extending from the eastern North Pacific (ENP) into the tropical Atlantic in late summer (Wang and Enfield 2001: Wang and Enfield 2003, henceforth WE01, WE02 respectively). Moreover, the interannual variations in its size are comparable with its average extent in summer. Interannually, the largest warm pools occur during the summer following most, but not all El Niño events and are associated with an anomalously warm tropical North Atlantic to the east (Enfield and Mayer 1997).

The WHWP is an important player in the Walker and Hadley circulations of the Western Hemisphere, replacing the boreal winter convective center over tropical South America as the summer heat source for the troposphere. During the months of its maximum development from June through October, the WHWP is a significant moisture source for the easterly low-level flow from the tropical Atlantic into the eastern North Pacific and the central United States (Bosilovich 2002). It seems likely that the largest variations in warm pool size and intensity (warmth) constitute a key factor in predicting boreal summer climate fluctuations in the Western Hemisphere.

The mechanisms for anomalous warm pool growth have not been determined although numerous studies have implicated the surface flux anomalies associated with North Atlantic trade wind departures as explaining sea surface temperature extremes in the tropical North Atlantic (e.g., Enfield and Mayer 1997). To fully resolve this question requires a study of the near-surface heat balance of the warm pool. A simple slab model

of the annual mean balance was done by Wang and Enfield (2003) with the total oceanic heat flux divergence as a residual. However such an approach is highly simplified by the combining of the ENP and Atlantic subregions together, and rendered uncertain by the undetermined ocean fluxes and the wide discrepancies between estimates of the net surface flux of the order of 100 Wm^{-2}. By considering the annual mean (steady state) heat balance of the western Pacific warm pool volume surrounded by an isothermal surface, Niiler and Stevenson (1982) were able to separate the diffusive ocean flux divergence from that of the advective terms, because the latter sum to zero over the oceanic isothermal surface by continuity. Toole et al. (2004, henceforth T04) examined the same balance for the Pacific, Atlantic and Indian Ocean warm pools but with a time-variable heat storage term so as to investigate the temporal behavior of the balance without the uncertainty of advective fluxes. In this paper we apply the T04 approach but with a more detailed focus on the annual cycle of the WHWP and its subregional components and by using multiple hydrothermal and surface flux data sets plus several isothermal surfaces to better estimate the temporal and geographical variations and their uncertainties.

After explaining our data and methods in section 2, in section 3 we describe the terms of the heat equation in more detail and in section 4 we perform a time variable version of the Niiler and Stevenson (1982) bubble analysis, generating estimates of the diffusion term a a residual. In section 5 we introduce the residual estimates of diffusive flux divergence into a heat balance for fixed slab layers in the four subregions obtaining a residual estimate of the advective heat flux divergence. In section 6 we make direct estimates of the vertical and horizontal advective heat flux divergence for the GoM and

ENP regions using the Ekman divergence ($f^{-1}curl\boldsymbol{\tau}$) and surface drifter data, respectively. These are compared to the residual estimates from the slab-layer analysis in section 7, where we also discuss our results generally. Our results and conclusions are summarized in section 8.

2. Data and methods

In what we call a "bubble analysis", we consider the heat balance within a three dimensional ocean volume bounded by the sea surface (A_S) and an oceanic isothermal surface (A_T) by estimating all but the rightmost term in the modified heat equation from which heat advection across the isothermal boundary has disappeared:

$$\underbrace{\frac{d}{dt}\iiint \rho c_p (T - T_o) dv}_{A} = \underbrace{\oiint_{A_S} Q_{NET}\, ds}_{B} - \underbrace{\oiint_{A_T} Q_{SWP}\, ds}_{C} + \underbrace{\oiint_{A_T} Q_{DIF}\, ds}_{D} \qquad (1)$$

(see T04 for derivation) where T is the water temperature, T_0 is the bounding temperature, ρ and c_p are the density and heat capacity of seawater, respectively and Q denotes a flux of heat through a surface. Term A is the diabatic change in heat storage, comprised of the total change minus the adiabatic change due to the change in volume. Term B is the net heat flux (Q_{NET}) across the sea surface; term C is the shortwave radiative flux that penetrates through the isothermal surface to the colder water below (Q_{SWP}); and term D is the total (horizontal plus vertical) diffusive heat flux (Q_{DIF}), which in the bubble analysis is estimated as a residual.

Our analysis strategy is based on two of the greatest strengths of the bubble approach. First, as already noted, the advective contributions to the heat balance are eliminated, ridding us of one of the most uncertain terms in the generalized ocean heat equation. Second, for an enclosed volume surrounded by colder water the diffusive term must be

negative (out of the volume), thus providing us with a most valuable constraint on the results. We use this constraint to disqualify two of the surface flux data sets and thus narrow the uncertainty in term *B*.

To assess the sensitivity of the heat storage term (*A*) to the ocean thermal analysis, we use two gridded hydrothermal (T(x,y,z)) climatologies: World Ocean Database 2001 (WOD01, Conkright et al. 2002) and the Fleet Numerical Oceanographic Center's (FNOC) Generalized Digital Environmental (GDEM) product (Teague et al. 1990). Because these products are based mostly on the same raw hydrographic data, differences reflect the impact of data handling, namely, processing, quality control, interpolation, averaging, gridding and such. Except in certain summary tables (where results for both are shown), the results shown will be for the WOD01 data.

To assess the effect on the analysis of the isotherm depth relative to the stratification — and of the different areas enclosed by the isotherms — we repeat the calculations for three convenient isotherms: 27.5°C, 28.0°C and 28.5°C. The ENP and Atlantic portions of the WHWP are dealt with as separate bubbles. At the lowest temperature (27.5°C) the ENP portion of the warm pool connects to the much larger Indo-Pacific warm pool via the North Equatorial Countercurrent (NECC) along 5-10°N. This also occurred in the T04 study (which used 27.0°C), preventing that analysis from isolating any conclusions regarding the ENP region. To avoid this problem we have used the WOD01 hydrothermal data and the Pacific drifter data to estimate the zonal advective heat flux through the 120°W meridian along the narrow zonal swath of the North Equatorial CounterCurrent (NECC). The small error introduced by neglecting that flux can be estimated as $Q_{ERR} = \rho c_p M_X (T_{120} - T_0)/A$, where M_X is the eastward transport bounded by T_0, and T_{120} is

the average temperature of the section through which it flows. For the ENP subregion (T_0 = 27.5°C) we add this correction to the right side of (1). The bubbles bounded by the 28.0°C and 28.5°C isotherms are never joined with the western Pacific and thus do not require this correction.

At certain times of the year, all three isotherms include Atlantic extensions of the volume east of the core warm pool in the Caribbean, especially at the lowest bounding temperature. These extensions sometimes include separated volumes (e.g., off the coast of Brazil), most of them too small to bias any conclusions about the larger contiguous warm pool. In the late summer, however, there is a large extension spanning the entire tropical North Atlantic to west Africa, while another large region of the equatorial Atlantic including part of the Gulf of Guinea is included as a separate volume that develops in the boreal spring. This volume is included in the Atlantic bubble calculations.

The term subject to the greatest error is the net surface flux (B), with very large differences between a number of available Q_{NET} estimations, even though most of them are based on the same source of data (COADS, Woodruff et al. 1998). The surface flux data sets we use here are the da Silva constrained and unconstrained climatologies (DSC and DSU, respectively, da Silva et al. 1994), Oberhuber (OBH, Oberhuber 1988), Southamption constrained (SHC, Grist and Josey 2003), Southamption unconstrained (SHU, Josey et al. 1998), NCEP/NCAR global reanalysis (NCEP, Kalnay et al. 1996), and the European Centre for Medium Range Weather Forecasting (ECMWF) 15-year global reanalysis (ERA15, Gibson et al. 1997). These data sets and the the periods for their climatologies, used in this analysis, are summarized in Table 1. The first five are based on standard marine observations; the last two are atmospheric global circulation

model (AGCM) integrations with assimilated historical data. In the constrained versions (DSC, SHC), parameterizations are adjusted so that Q_{NET} integrates to zero over the world ocean and is consistent with the oceanic net heat transport convergence between parallels.

Subsurface shortwave irradiance attenuation is estimated from satellite ocean color data (SeaWiFS) using several algorithms, yielding an attenuation coefficient K_a that is spatially and temporally varying over the WOD01 grid and for all months of the year. The K_a estimates are compared to the historical optical water type standards (constants in time and space) set by Jerlov (1976) and the most appropriate algorithm is adopted. The selected time-space variable ate nuation coefficient is then applied to the incoming shortwave radiative flux Q_{SWR} to obtain the estimated shortwave penetration (term *C*), where Q_{SWR} corresponds to whichever data set is used for term *B*.

We compute the slab-layer heat budgets for four subregions of warm pool development having volumes of constant dimensions: the eastern North Pacific (ENP), the Gulf of Mexico (GoM), the Caribbean (CBN) and the equatorial Atlantic (EQA) (Figure 1). These calculations are done for the three-month seasons in which the warm pool is best developed in those subregions. The WOD01 hydrothermal data and the unrejected surface flux climatologies are used as in the bubble analysis to estimate terms *A*, *B* and *C*. The diffusive flux estimates (term *D*) corresponding to the surface fluxes are input from the bubble analysis, also averaged over the same months and regions. Because the slab calculations do not eliminate the advection terms in the heat equation as occurs in the bubble analysis, these are estimated as a collective total in the residual (vertical plus horizontal).

3. Quantification of terms used in the heat equation

a. Heat storage

Figure 2 shows the annual cycle for the T_0 = 27.5°C, 28.0°C and 28.5°C isotherms for the tropical North Atlantic and eastern Pacific, used to define the WHWP in this study (WOD01, solid). For comparison, the GDEM version of the 28.0°C isotherm is also shown (dotted). The WHWP is insignificant during the winter months (January-February) with only small features in the ENP and EQA regions. The ENP warm pool begins to form off the west coast of Central America in March and attains maximum development in April-May. As the ENP warm pool decreases in size in June and July, the Atlantic warm pool begins to develop in the GoM and is fully developed there in July and August. In August the warm pool expands southward into the Caribbean, while in September and October it is largest and covers all of the Caribbean and much of the tropical North Atlantic. We will refer to the three-month seasons of April-June, July-September and August-October as the ENP, GoM and CBN phases of maximum development, respectively. The EQA region is best developed in March-May, although vestiges of it exist all year round. These regions and seasons will be specifically analyzed in sections 5 and 6.

To understand how the various warm pool defining volumes relate to their regional shallow stratifications, Table 2 summarizes the three-month mean isotherm depths (Z_T) and mixed layer depths (MLD, defined by T(MLD) = T(0) – 0.5°C) averaged over the appropriate warm pool segments during the phases of maximum development in each region. The calculation for each subregion is restricted to only the grid points within each polygon (Figure 1) where $T>T_0$. For the T_0 = 27.5°C isotherm, this is most or all of the polygon area; for T_0 = 28.5°C it is often only a fraction thereof (compare Figures 1 and 2). Even though the areas averaged can be quite different within a given subregion, the

mixed layer depth shows little sensitivity to the area of the defining isotherm, except in the EQA. The mean mixed layer depth is in general between the 28.0°C and 28.5°C depths except in the EQA where it increases with the area of the defining isotherm. Both the warm pool and its associated mixed layer are deepest in the CBN region and shallowest in the ENP and GoM.

Figure 3 shows maps of the WOD01 isotherm depth and MLD for T_0 = 28.0°C, further illustrating their similarity. Several geographic features stand out. One is the dipole of isotherm depth off Central America in May. This is a remnant of the dynamical forcing of the thermocline by the winter mountain-pass wind jets over the Gulfs of Tehuantepec and Papagayo (McCreary et al. 1989). The deep region south of the Greater Antilles, strongest in September, is clearly the reason for the larger average isotherm depths in the CBN region (Table 2), and it stands in contrast to the shallow region along the north coast of South America where the easterly winds produce persistent coastal upwelling. The deep region is of particular importance to Atlantic hurricane forecasters because of its large storm development potential (heat reservoir). Finally, in September the warm pool extends well into the tropical North Atlantic near 10°N in association with the north-shifted summer Intertropical Convergence Zone (ITCZ).

Figure 2 shows that the WOD01 and GDEM climatologies are similar for T_0 = 28.0°C but that differences do occur and the area enclosed is sometimes greater and at other times smaller for one than for the other. From Table 2 we see that the GDEM depths are usually slightly smaller for T_0 and slightly larger for MLD. This is mainly due to the finer vertical resolution in GDEM. We have found that the small horizontal and vertical differences in defining volumes between the two hydrothermal analyses do not have a

large effect on the heat storage calculations. Therefore, uncertainties in the heat storage term are most likely related to the unknown effects of the uneven distribution of hydrographic data.

b. Net surface flux

Table 3 summarizes the averages of Q_{NET} for the same subregions and seasons as shown in Table 1, for all seven surface flux climatologies, ranked from left to right according to the average amount of heat absorbed by the ocean annually in the Western Hemisphere tropics (30°S-30°N, Africa to 120°W). Figure 4 shows the distribution of Q_{NET} for the two surface flux climatologies that comprise the extremes (DSU, ERA15) and their difference. At one end of the range the DSU and SHU data sets are very close and give the greatest amount of net heat flux. At the other extreme are the two reanalyses (NCEP and ERA15) with the least absorbed heat. In some regions, such as off Brazil in the South Atlantic and in the subtropical North Atlantic, the differences between extremes are nearly 150 Wm^2. Ranges of 70 Wm^2 are typical over the CBN, GoM and EQA regions, while in the ENP the range is slightly less. Averaged over the Western Hemisphere tropics, the largest contribution to the differences in Q_{NET} (between climatologies) comes from the incoming shortwave radiation and the next largest from the latent heat flux (not shown).

c. Radiative penetration

In Table 4 we compare several different strategies for estimating the radiative flux that penetrates through the bottom of the warm pool (Q_{SWP}). One is to apply the irradiance attenuation coefficient appropriate to one of the Jerlov water types (I, II, or III, constant in time and space) to the incoming shortwave radiation. This is the most common approach adapted in other studies. However, several algorithms now exist for deriving

space and time variable attenuation coefficients from satellite color imagery, a more precise method for a warm pool boundary that changes with respect to the optical water type distribution. The three satellite algorithms tested here are by Morel (1988), Ohlmann (2003) and McLain et al. (2002), each of which is computed for the WOD01 grid points, applied to the Q_{SWR} values at the same grid points, and averaged over the warm pool regions and seasons. Figure 5 shows the distribution of the irradiance attenuation depth (Z_A) derived from the SeaWiFS attenuation coefficient at 490nm (K490 hereafter) (McLain et al. 2002), with the Jerlov (1976) water types superimposed.

From Figure 5 we see that the GoM has the clearest water (IA; $Z_A > 20$m), followed closely by the CBN (IA to IB; 15m < Z_A < 25m), while the ENP and EQA are most turbid (II; $Z_A < 20$m). The K490 algorithm gives patterns that are optimally consistent with the Jerlov water types shown (Figure 5) and give shortwave penetrative fluxes that are closest to those inferred from Jerlov's classification (Table 4). If the historical observations are correct, then it appears that among the three satellite methods the K490 estimates are the most reliable. Therefore in this paper we have elected to use the K490 satellite method as being most consistent with direct observations while offering resolution of temporal and spatial variations. For a given depth and incoming shortwave flux, we estimate that the K490 estimates of the shortwave penetrative flux may have an uncertainty of ±5 Wm^{-2}. Larger errors are more likely to result from errors in the surface flux or the local bubble depth.

4. Bubble analysis

Figures 6-7 and 8-9, respectively, summarize the bubble-analyzed heat balances for the Pacific and Atlantic portions of the warm pool. Shown in the top panel are the annual

cycles of the area-averaged storage rate and sea surface temperature (WOD01); in the middle panel, Q_{NET} minus Q_{SWP} for the seven surface flux climatologies; and in the bottom panel the resulting residuals, or estimated total diffusive flux (Q_{DIF}) corresponding to the respective surface flux climatologies. For each region the analysis is done separately for the coolest (27.5°C; Figures 6, 8) and warmest (28.5°C, Figures 7, 9) defining isotherms. In Table 5 the residuals (Q_{DIF} estimates) for both hydrothermal climatologies and all three defining isotherms are shown for the four subregions and their respective seasons of maximum development. The differences between the WOD01 and GDEM climatologies are within ±5 Wm^{-2} with no clear bias in either direction, and therefore the choice of hydrothermal climatology for defining the warm pool volume has little impact on the resulting balance.

a. Description of the heat balance

Growth of the warm pool (dH/dt) in the ENP region is restricted to the February-April period, prior to the spring maximum in SST (Figure 6). The surface heat flux absorbed shows a clear annual cycle for the 27.5°C isotherm, which is present year-round. Only a portion of the annual variation can be seen for 28.5°C, which is only present during the summer months (Figure 7). For 27.5°C the very similar DSU and SHU climatologies give the greatest absorbed heat, ranging from 25 Wm^{-2} or less in October-December to 40-80 Wm^{-2} in the February-September time frame. The least heat absorbed is for ERA15 followed closely by NCEP with a net heat loss in winter. The Oberhuber and the constrained data-based climatologies (OBH, DSC, SHC) fall in the lower half of the range defined by the latter extremes. All the annual cycles are similar except for NCEP, which shows considerably more absorbed heat in summer than in winter.

The Pacific residual term (27.5°C), or estimated total diffusive flux (Q_{DIF}), tends to reflect the annual cycle in surface heat gain but is slightly modified by the smaller annual cycle of the storage rate. In November-February Q_{DIF} varies from a -25/-45 Wm^{-2} range (DSU, SHU) to +10/+25 Wm^{-2} (NCEP, ERA15), while for March-October it varies from -50/-60 Wm^{-2} (DSU, SHU) to -10/+20 Wm^{-2} (ERA15). Over the same periods, all the Q_{NET} data sets (except for NCEP) yield a similar 15 to 20 Wm^{-2} seasonal contrast in Q_{DIF}, which leads us to surmise that the seasonality, though only moderate, is probably marginally significant.

The ERA15 data set yields unrealistic (non-physical) or unlikely ENP residuals for 27.5 °C that are positive (implied diffusive heat gain) for most of the year. Similar, positive residuals occur for NCEP during the winter months but because of the uniquely strong seasonal cycle of NCEP Q_{NET}, the summer months have large negative values. The remaining climatologies yield residuals that bracket a physically possible range for Q_{DIF}, from near-zero (OBH, SHC) in winter to more than 50 Wm^{-2} of diffusive heat loss from late spring through summer (DSU, SHU). It is difficult to render a similar judgment for 28.5°C because most of the winter months are missing. Finally, we note that for the warm pool season the residuals for the 28.5°C and 27.5°C isotherms vary within the same ranges, suggesting that the estimate of Q_{DIF} is insensitive to the warm pool depth (18-28 m), which brackets the mixed layer depth (21-22 m) (Table 2).

In the Atlantic (Figure 8), the 27.5°C results have an unrealistic discontinuity in Q_{NET}–Q_{SWP} and Q_{DIF} between December and January, and a trend between those extremes during the year. From Figure 2 we can see the reason for the discontinuity: starting in January and for the first half of the year, the 27.5°C Atlantic warm pool is dominated by

the Atlantic east of 40°W (EQA), while in the latter half of the year through December it is dominated by the western Atlantic, including the GoM and CBN. Hence, rather than being a physically meaningful annual cycle of the heat balance in a given region, the figure represents differences between the two sides of the Atlantic. As before, the NCEP and ERA15 climatologies yield a physically inconsistent range of Q_{DIF} estimates while the remaining estimates range from +10/+15 Wm^{-2} (DSC, SHC) to -55/-65 Wm^{-2} (DSU, SHU) in Mar-May (eastern Atlantic) and from -10/-15 Wm^{-2} to -40/-50 Wm^{-2} in August-October (western Atlantic) (Table 5). Although DSC and SHC give positive residuals in November-December for 27.5°C (Figure 8), these are months when the warm pool areas are small and may yield less stable balances, while the DSC and SHC values during the warm pool seasons give clearly acceptable residuals.

For the 28.5°C warm pool (Figure 9) the eastern and western portions of the Atlantic are cleanly separated into the boreal spring and fall months, respectively. As in the Pacific, the residual estimates are insensitive to the defining isotherm. For 28.5°C the DSC and SHC climatologies give slightly positive residual values in September and October when the Caribbean is dominant but are quite satisfactory during the ENP and EQA warm pool seasons (Figures 7, 9).

b. Narrowing the possible balance

The numerical averages in Table 5 for the subregions and their respective warm pool seasons confirm that the ERA15 Q_{NET} gives non-physical residuals for all regions, while NCEP is clearly unrealistic in the intra-Americas Sea region (GoM, CBN). Some positive residuals occur for DSC and SHC, but they are not large and the averages for the warm pool seasons are acceptable (negative). Hence, we can only disqualify the NCEP and

ERA15 surface fluxes as being physically inconsistent in the WHWP region based on sign.

The total diffusion inferred from the remaining five surface flux climatologies falls into two groups: the DSU and SHU climatologies yield much greater diffusive cooling (-35 to –55 W/m^2) than do the OBH, DSC and SHC climatologies (-5 to –25 W/m^2). To check on which of these two ranges seems most reasonable, we consider the Indo-Pacific warm pool for which far more observational evidence exists, including results from the extensive TOGA-COARE experiment. The consensus of most studies to date is that vertical diffusion there accounts for cooling rates of 0 to –20 W/m^2, while horizontal diffusion is generally small west of the central equatorial Pacific (e.g., Ramanathan et al. 1995). However, the Indo-Pacific warm pool is much deeper (50-60 m) than the WHWP, which makes the two regions difficult to compare in this manner. Therefore, we apply our bubble analysis to the Indo-Pacific warm pool west of 120°W (subtracting the 120°W advective correction described in section 2) and find total diffusive coolings of –45 to –55 W/m^2 (SHU and DSU) and –10 to –20 W/m^2 (OBH, SHC and DSC). Our results for DSU and SHU are consistent with those of Toole et al. (2004) who used the SHU climatology. The OBH, SHC and DSC surface fluxes yield results similar to those for the WHWP and also to the consensus range from Indo-Pacific observations. By this measure, previous studies of the Indo-Pacific warm pool combined with our own analysis indicate that the constrained (SHC and DSC) and Oberhuber surface fluxes are in the correct range for the tropics and that the unconstrained data sets yield diffusion rates that are too high.

c. Surface forcing of the warm pool

As seen in the bubble heat balance analysis, the advective flux divergence disappears and the residual estimate of diffusion does not suggest any time variability that can relate to the onset and demise of the warm pool. Hence, while Q_{DIF} is needed for closing the overall budget, the annual cycle of warm pool development must be related to the components of the net surface heat flux. Therefore, we wish to look at the component surface fluxes and their relation to the warm pool cycle. The relevant terms are shown in Figures 10 and 11 for the ENP and Atlantic warm pools, respectively, using only the 27.5°C bounding isotherm to compute the area-averaged SST, heat storage rate and fluxes. To make the presentation less confusing we do not include the net longwave flux nor the sensible heat flux, both of which have only small seasonal variations with no apparent relevance to warm pool development. Moreover, since it is only the seasonal variations we are interested in, we have removed the annual mean fluxes. To minimize the biasing effects of surface flux parameterization errors on the calculations, we use only Q_{NET} for the Southampton constrained data set, one of the three selected in section 4b. The conclusions are unaffected by using either of the other two surface flux data sets.

For the ENP (Figure 10), the sharp SST maximum in April-June is preceded by February-April maxima in Q_{NET} and storage rate, and followed by minima of same in May-July. Also, we see that Q_{NET} is mimicked most closely by the solar radiation (Q_{SWR}) in both phase and amplitude, and by latent heat in phase but with smaller amplitude (middle panel). The onset of the large shortwave flux (Q_{SWR}) in late winter is clearly controlled by a sharp increase in solar radiation at the top of the atmosphere (Q_{TOA}) related to the solar declination (bottom panel). However, the subsequent decrease in April-May is mainly caused by a concurrent increase in cloud cover. Evaporative heat

loss Q_{EVP} is minimum in winter (largest values of the seasonal anomaly) when the warm pool is coolest, and it becomes maximum (negative values) in May-July after the warmest SSTs are established. Examination of the wind speeds (not shown) does not suggest that evaporation responds to winds in the context of the annual cycle, rather, to the SST. The penetrative shortwave flux (Q_{SWP}) appears to be passive, presenting maximum loss in winter when the warm pool is small and shallow, and minimum loss in April-June when the warm pool is largest and deepest. Hence, it seems clear that the warm pool first develops in response to increasing solar radiation as the solar declination approaches zero in late winter. Then, as SST and the warm pool size approach their spring maximum, evaporation and convection increase, associated with the onset of the Mexican monsoon, and cloudiness also increases, so that both Q_{SWR} and Q_{EVP} contribute to the cooling and contraction of the warm pool. Less shortwave radiation penetrates the 27.5°C bubble as the warm pool grows and deepens, thus helping to persist the warm pool maximum.

The relationships in the Atlantic (Figure 11) are complicated by a strong double maximum in the warm pool, one in March-May associated with the equatorial Atlantic, the other in late summer centered over the Caribbean. As in the ENP, the SST maxima are preceded by respective maxima in Q_{NET}, dH/dt, and Q_{SWR}, and the incident shortwave radiation is controlled by the solar declination (Q_{TOA}). There are also increases in evaporative heat loss following the subregional warm pool maxima, but they are not as large as in the Pacific. More than in the Pacific, the annual cycle of the Atlantic warm pool is dominated by solar declination in all phases of its evolution.

5. Slab-layer analysis

In this section we consider the heat balance of a slab volume of constant thickness within each of several subregions of the warm pool: ENP, GoM, CBN and EQA (Figure 1). For each subregional slab, the horizontal boundaries are defined by land (the coastal boundaries of the WOD01 grid) or by the approximate extent of the 28°C isotherm boundary during the season of maximum warm pool development in the subregion. The slab thickness is taken to be 30 m for convenience in using surface drifter data (15 m drogue depth) as an independent estimate of horizontal advection (next section). 30 m is not far from the warm pool depth as defined by the 27.5°C isotherm and the bubble analysis shows that the residual estimates of diffusive flux are not sensitive to the volume depth (Table 5).

In combination with the bubble analysis just described, the slab-layer procedure offers further advantages for understanding the heat balance. For a slab, the heat balance equation (1) now contains an additional term $\oiint_{A_T} Q_{ADV} ds$ for the combined vertical and horizontal heat advection through the bottom and side boundaries, respectively. Terms, *A*, *B* and *C* are calculated as before for the slab surface areas but from the bubble analysis we can now exclude the all of the surface flux climatologies except for DSC, SHC and OBH. For term *D* we use the residual estimates of Q_{DIF} from the 27.5°C bubble analysis corresponding to each of the retained surface flux estimates. Besides having a warm pool depth closest to 30 m, 27.5°C comes closest to including the entire slab region during the respective seasons of maximum warm pool development. We use the average seasonal value of Q_{DIF} appropriate for the season of maximum warm pool development within each subregion (Table 5). The residual from the slab analysis Q_{RES} is ostensibly an estimate of the total advective contribution to the balance Q_{ADV}. However, because the

residual also contains the sum of all errors in the storage and surface flux terms, one cannot accept them at face value as representing the advective heat flux divergence. Hence, in the next section we will make direct estimates of the advective contribution for comparison.

The results are summarized in Table 6. Here we do not include estimates for the 28.5°C isotherm because the depth of 28.5°C is the least appropriate for the 30 m slabs (Table 2) and the portion of the ENP slab covered by water warmer than 28.5°C is too small. The corresponding values of Q_{DIF} (term D in the slab balance) are repeated from Table 5. Because in the bubble analysis the magnitude of Q_{DIF} varies in proportion to the heat absorbed but with opposite sign, differences in terms B and C (between the three surface flux data sets) are largely offset by corresponding differences in the bubble estimate for Q_{DIF} (term D). This causes the residual estimates of Q_{ADV} for the slabs to be stable and collapse on a relatively narrow range of values. The slab balances yield less than -10 W/m^2 of estimated total advective cooling for the ENP and CBN, and somewhat more cooling for GoM and EQA.

6. Advective heat flux divergence

One would like to independently estimate the advective contributions to the heat balance, so as to determine whether the balance so far constructed from the combined bubble and slab analyses is reasonable. Of the four subregions considered, the ones that offer the best prospects for such estimates are the ENP and GoM. The former has a relatively large amount of drifter data (with 15-meter drogues) that have accumulated over a 20-year period; the latter because, although the drifters are much less plentiful, they are constrained to go through the narrow Yucatan Channel and Florida Straits

(between Key West and Cuba). Too little is known about the transports through the Antillean passages to attempt an estimate for the Caribbean, and much less data are available to construct estimates for the EQA subregion.

a. Gulf of Mexico

The annual mean 15 m drifter flows through the Yucatan Channel and Florida Straits are shown in Figure 12 (Lumpkin 2003). More than 90% of the drifter data are for 1999-2003 and provide about 300 drifter-days of information for the constricted domain of each channel. This is about equal to the drifter coverage spread over the much larger domain of the subtropical North Atlantic but considerably less than that afforded by 20 years of drifter data in the ENP region. The cross-channel distribution of flow through the Yucatan Channel looks remarkably similar to that shown by the best measurements to date from a two-year cross-channel array of current meters and acoustic Doppler profilers (Sheinbaum et al. 2002) (their Figure 2a). The annual average 0-30m through-channel transport is $M_Y = 3.1$ Sv and $M_F = 3.6$ Sv for the Yucatan and Florida Straits, respectively, and the corresponding annual average cross-channel SSTs (Reynolds and Smith 1994) are $T_Y = 27.6$°C and $T_F = 26.8$°C. During the warm pool season (July-September) the down-gulf SST gradient becomes slightly reversed (0.3°C warmer at the Florida Straits). To estimate the horizontal heat advection through the channels we bin the perpendicular component of the 15 m drifter velocities into quarter-degree cross-channel boxes as shown in Figure 12 and assume that they are the averages for the 0-30 m layer. These are multiplied by the Reynolds and Smith (1994) SST product interpolated to the bins and the product is integrated across the channel.

We estimate the vertical component of transport through the base of the slab from two climatologies of wind stress curl (da Silva and Southampton) interpolated to the WOD01 hydrothermal grid:

$$M_{30} = f^{-1} \oiint_A \nabla \times \boldsymbol{\tau} \; ds. \tag{3}$$

The vertical advective heat flux across the base of the slab is estimated from the area integral of the product of one-degree gridded wind stress curl (M_{30}) and WOD01 temperatures (T_{30}).

There is good agreement between the wind stress climatologies. Anticyclonic winds dominate the Gulf from late winter through summer and fall, yielding up to 1 Sv of downwelling (in July), while weak upwelling prevails from October through January for an annual average downwelling of -0.4 ~ -0.5 Sv. This implies that the average annual Yucatan transport must exceed the Florida transport by a similar amount, which is opposite to the drifter result. However, although the drifter estimates may contain appreciable errors, the windstress curl does not resolve vertical velocities in the narrow coastal zones surrounding the WOD01 1°x1° grid. Upwelling is known to occur seasonally around the Gulf, over the shallow Campeche banks, the northeastern Gulf coast and the west Florida shelf. Compensating coastal downwellings probably also occur (Virmani and Weisberg 2003). It is thus impossible to accurately close the mass balance or to know which of the competing mass fluxes is more correct.

The mass imbalance M_Δ remaining from the independent estimates of horizontal and vertical mass transport is comprised of measurement error and unresolved mass transports. This imbalance is applied as a correction term $Q_\Delta = \rho c_p M_\Delta T_\Delta / A$, where A is the slab area and T_Δ is the average temperature of the slab volume (since we don't know

how M_Δ is distributed over the surfaces of the slab). The horizontal, vertical and correction fluxes are summed to estimate the total advective heat flux divergence. Over the year, total advection accounts for about +8 W/m^2 of warming during the winter months largely due to the downstream temperature decrease and the predominant downwelling. During the warm pool season (July-September) there is a net cooling of about -5 W/m^2 due to the reversal of the down-gulf SST gradient.

Although the errors in the measured transports are not small, the estimate of total heat flux divergence is stable within a narrow uncertainty range due to the application of the continuity correction term. Large changes in the measured transports are taken up by the correction term and applied at a temperature that is only a few tenths of a degree different. For example, if the value of T_Δ is taken to be T_{30} or the SST (the possible extremes), our estimate changes by only 2 to 3 W/m^2 one way or the other. In other words, if the true value of either component transport were known to differ by M_Δ from our estimates, the resulting total advective heat flux divergence would be essentially unchanged. The uncertainty of the individual horizontal and vertical component heat flux divergences is much larger due to the lack of a transport constraint.

b. Eastern North Pacific

For the ENP, the total advective heat flux divergence ofthe slab-layer is estimated in similar fashion. The horizontal component is estimated from the perimeter integrated product of temperature and the perpendicular drifter flow, both averaged for one-degree squares around the slab perimeter. As for the GoM slab, the vertical transport through Z = 30 m is estimated from the area-integrated product of wind stress curl and slab-base temperature, and a correction term is applied using the error transport computed from the mass imbalance between the independently estimated vertical and horizontal transports,

together with an average temperature for the volume. From this we find that the ENP region is cooled by total advection throughout the year, ranging from ~ –10 to -15 W/m^2 in winter to near zero in summer and about -2 W/m^2 during the warm pool season (April-June).

7. Discussion

The overall balance is shown in Table 7 for the four subregions (Figure 1) with ranges combined and summarized for the 28.0°C and 27.5°C isotherms and based on the three most acceptable surface flux climatologies (OBH, SHC and DSC). The three surface flux climatologies yield a surface ocean warming of +20 to +30 W/m^2 that is partially offset by –5 to –25 W/m^2 of cooling through combined horizontal and vertical turbulent diffusion. The balance is closed by an estimated cooling (zero to -10 W/m^2) by the total advective heat flux divergence Q_{RES} (slab residual) in the ENP and CBN, and –5 to –15 W/m^2 for the GoM and EQA. For the GoM and ENP subregions there is remarkably good agreement from direct observations (wind stress and drifters) for the total heat advection Q_{ADV}, as compared with the slab-layer residuals, Q_{RES}. This gives us confidence in our results for those regions and for the others as well and confirms our selection of surface flux data sets.

We cannot say very much about the horizontal versus vertical components of Q_{DIF} and Q_{ADV}. It seems unlikely that horizontal diffusion is important in the Gulf of Mexico or Caribbean. In the Gulf of Mexico the only open boundaries have strong steady flows. Although North Brazil Current eddies impinge on the Caribbean from the east, the zonal temperature gradients between the Caribbean and the open Atlantic are generally small.

Hence the total diffusion estimates in Table 7 are likely to be primarily vertical. Horizontal diffusion may be more important in the ENP and EQA regions, the former due to the presence of the Tehuantepec and Papagayo eddies in the late winter and early spring, the latter due to tropical instability waves near the equator.

Inclusion of the mass imbalance correction yields narrow and stable estimates of the total observed advective heat flux divergence Q_{ADV} that agree with the slab-layer residuals (Table 7). However, efforts to estimate the horizontal and vertical components of Q_{ADV}, through assumptions of how the mass imbalance correction is partitioned between the bottom and sides of the slabs, result in unstable results and large ranges that preclude any useful conclusions. We cannot discard the possibility that the two components have considerably larger but opposing values.

8. Summary and conclusions

We have used two hydrothermal data sets to define warm pool volumes and their heat storage rates for three defining isotherms and have constructed warm pool heat budgets using seven of the most commonly used surface heat flux climatologies. The problem of estimating the radiative heat loss through the bottom of shallow warm pools is addressed by using a spatially and temporally varying irradiance attenuation inferred from satellite color imagery, according to an algorithm (McLain et al. 2002) that is most consistent with historical direct measurements (e.g., Jerlov 1976).

The WHWP is comprised of four geographically separate subregions with distinct or overlapping seasons of maximum development. The eastern North Pacific (ENP) and equatorial Atlantic (EQA) are best developed in the boreal spring, while the Gulf of Mexico (GoM) and Caribbean dominate during the early and late summer, respectively.

Warm pool depths are similar to the mixed layer depth (20-40 m) and are much less than for the Indo-Pacific warm pool (50-60 m).

Using a time-dependent variation of the Niiler and Stevenson (1982) heat balance for a constant warm pool bounding temperature we have been successful in narrowing the number of surface flux climatologies that are acceptable for the Western Hemisphere tropics, from seven to three. The two climatologies based on the NCEP and ERA15 reanalyses put too little heat into the warm pools, resulting in non-physical (positive) residual estimates of the diffusive heat flux divergence. Of the remaining five climatologies, the unconstrained fluxes (SHU and DSU) err on the opposite side, putting too much heat into the ocean and yielding diffusive cooling rates that are inconsistent (too large) with observational evidence for the Indo-Pacific warm pool. We conclude that heat balance studies of warm tropical ocean regions are best-served by the globally constrained surface flux data of da Silva and Southampton. We cannot extend these conclusions to other regions of the globe such as the cold tropics (e.g., southeast Pacific) or the extratropics. For modeling purposes the globally constrained Southampton surface fluxes are currently the best choice because the adjustments are distributed to the component fluxes, whereas the da Silva constraint is applied only to the net flux.

The remaining surface flux data sets of da Silva and Southampton (DSC, SHC, constrained) and Oberhuber (OBH) have a much narrower range of surface warming ($+25 \pm 5$ W/m^2) over the subregional slab layers, with associated bubble residual estimates of total diffusion of -5 to -20 W/m^2 (± 5 W/m^2) depending on the subregion considered. When these are then input into a slab-layer balance, we obtain relatively narrow estimates of cooling by total advective heat flux divergence of -2 to -14 W/m^2 (± 5 W/m^2). The

latter are confirmed by more direct estimates using wind stress data and drifters for the GoM and ENP regions.

We conclude that the bubble (constant bounding temperature) and slab-layer (constant volume) approaches to the heat balance, when combined, are very effective at reducing the large uncertainty presented by the many surface flux climatologies presently available. By disqualifying the unacceptable surface flux data sets, these methods allow us to infer relatively stable and narrow ranges for the total diffusive and advective heat flux divergences.

Using the inferential (bubble and slab) methods it is not possible to separate the ocean heat flux estimates into their vertical and horizontal components. Doing so for vertical and horizontal advection will require direct measurements adequate to reduce the uncertainty presented by mass imbalances. Doing so for the diffusive (vertical) fluxes may require appropriate microstructure measurements at key sites within the warm pool regions so as to determine the vertical diffusivities.

Acknowledgements. Our thanks to Drs. Rick Lumpkin and Ajoy Kumar for processing the drifter and SeaWiFS and to Drs. Rick Lumpkin and Claudia Schmid for their pre-submission reviews of the manuscript. This research was supported by the NOAA PACS/GAPP Program through awards under Cooperative Agreement NA67RJO149 to the Cooperative Institute for Marine and Atmospheric Studies.

References

Bosilovich, M. G., 2002: On the vertical distribution of local and remote sources of water for precipitation. *Meteorology and Atmospheric Physics*, **80,** 31-41.

Conkright, M. E., T. D. O'Brien, T. P. Boyer, C. Stephens, R. A. Locarnini, H. E. Garcia, P. P. Murphy, D. Johnson, O. Baranova, J. I. Antonov, R. Tatusko, R. Gelfeld, and I. Smolyar, 2002: World Ocean Database 2001, CD-ROM Data Set Documentation. Silver Spring, MD, National Oceanographic Data Center, 137 pp.

da Silva, A. M., C. C.Young, and S. Levitus, 1994: *Atlas of surface marine data 1994*. Vol. 1, *Algorithms and procedures*. *NOAA Atlas NESDIS 6*, US Dept. of Commence, 83 pp.

Enfield, D. B. and D. A. Mayer, 1997: Tropical Atlantic sea surface temperature variability and its relation to El Niño-Southern Oscillation. *Journal of Geophysical Research*, **102,** 929-945.

Gibson, J. K., P. Kållberg, S. Uppala, A. Hernandez, A. Nomura, and E. Serrano, 1997: ERA description. Re-Analysis (ERA) Project Report Series No. 1, 72 pp.

Grist, J. P. and S. A. Josey, 2003: Inverse Analysis Adjustment of the SOC Air–Sea Flux Climatology Using Ocean Heat Transport Constraints. *Journal of Climate*, **16,** 3274-3295.

Jerlov, N. G., 1976: *Marine Optics*. Elsevier Publlishing Company, 226 pp.

Josey, S. A., E. C. Kent, and P. K. Taylor, 1998: The Southampton Oceanography Centre (SOC) Ocean–Atmosphere Heat, Momentum and Freshwater Flux Atlas. Southampton Oceanography Centre Rep. 6, 30 pp.

Kalnay, E., M. Kanamitsu, R. Kistler, W. Collins, D. Deaven, L. Gandin, M. Iredell, S. Saha, G. White, J. Woollen, Y. Zhu, M. Chelliah, W. Ebisuzaki, W. Higgins, J. Janowiak, K. C. Mo, C. Ropelewski, J. Wang, Leetmaa, R. Reynolds, R. Jenne, and D. Joseph, 1996: The NCEP/NCAR 40-year Reanalysis Project. *Bulletin of the American Meteorological Society*, **77,** 437-471.

Lumpkin, R., 2003: Decomposition of surface drifter observations in the Atlantic Ocean. *Geophys. Res. Lett.*, **30,** 6-1 to 6-4.

McCreary, J. P., H. S. Lee, and D. B. Enfield, 1989: The response of the coastal ocean to strong offshore winds: With application to circulations in the Gulfs of Tehuantepec and Papagayo. *Journal of Marine Research*, **47,** 81-109.

McLain, C. R., J. R. Christian, S. R. Signorini, M. R. Lewis, I. Asanuma, D. Turk, and C. Dupouy-Douchement, 2002: Satellite ocean-color observations of the tropical Pacific Ocean. *Deep Sea Research II*, **49,** 2533-2560.

Morel, A., 1988: Optical modeling of the upper ocean in relation to its biogenous matter content (case I waters). *Journal of Geophysical Research*, **93 C9,** 10,749-10,768.

Niiler, P. P. and J. Stevenson, 1982: On the heat budget of tropical warm water pools. *Journal of Marine Research*, **40 (Suppl),** 465-480.

Oberhuber, J. M., 1988: An atlas based on the COADS data set: The budget of heat, buoyancy and turbulent kinetic energy at the surface of the global ocean.15, 199 pp.

Ohlmann, J. C., 2003: Ocean radiant heating in climate models. *Journal of Climate*, **16,** 1337-1351.

Ramanathan, V., B. Subasilar, G. J. Zhang, W. Conant, R. D. Cess, J. T. Kiehl, H. Grassl, and L. Shi, 1995: Warm pool heat budget and shortwave cloud forcing: A missing physics? *Science*, **267,** 499-503.

Reynolds, R. W. and T. M. Smith, 1994: Improved global sea surface temperature analysis using optimum interpolation. *Journal of Climate*, **7,** 929-948.

Sheinbaum, J., J. Candela, A. Badan, and J. Ochoa, 2002: Flow structure and transport in the Yucatan Channel. *Geophysical Research Letters*, **29,** 10:1-4.

Teague, W. J., M. J. Carron, and P. J. Hogan, 1990: A comparison between the Generalized Digital Environmental Model and Levitus climatologies. *J. Geophys. Res.*, **95 C5**.

Toole, J. M., H.-M. Zhang, and M. J. Caruso, 2004: On the time-dependent internal energy budgets of the tropical warm-water pools. *Journal of Climate*, **17,** (submitted).

Virmani, J. and R. H. Weisberg, 2003: Features of observed annual ocean-atmosphere flux variability on the west Florida shelf. *Journal of Climate*, **16,** 734-745.

Wang, C. and D. B. Enfield, 2001: The Tropical Western Hemisphere warm pool. *Geophysical Research Letters*, **28,** 1635-1638.

— —, 2003: A further study of the tropical Western Hemisphere warm pool. *Journal of Climate*, **16,** 1476-1493.

Weisberg, R. H., 1996: On the evolution of SST over the PACS region. *Abstracts of the 76th AMS Annual Meeting*, Atlanta, Georgia, Am. Meteor. Soc., 378.

Woodruff, S. D., H. F. Diaz, J. D. Elms, and S. J. Worley, 1998: COADS release 2 data and metadata enhancements for improvements of marine surface flux fields. *Physics and Chemistry of the Earth*, **23,** 517-526.

Table 1. The Q_{NET} data sets used in this study, the time periods for the climatologies used, and the original gridding schemes that were interpolated to the WOD01 grid in this paper.

Data set (Q_{NET})	Symbol	Time period	Grid
ECMWF 15-year reanalysis	ERA15	Jan-1979 ~ Dec-1993	2.5° x 2.5°
NCEP/NCAR reanalysis	NCEP	Jan-1949 ~ Nov-2003	~ 2° x 2°
Da Silva et al.	DSU, DSC	Jan-1945 ~ Dec-1989	1° x 1°
Southampton	SHU, SHC	Jan-1980 ~ Dec-1993	1° x 1°
Oberhuber	OBH	Jan-1950 ~ Dec-1979	2° x 2°

Table 2. Three-month mean isotherm depths (Z_T) and mixed layer depths (MLD) averaged over the appropriate subregional warm pool segments during the phases of maximum development in each region. The calculation for each subregion is restricted to only the grid points within each polygon (Figure 1) where T is greater than the temperature defining the warm pool (T_0). Values in the left and right columns are calculated from the $T(z)$ profiles of the WOD01 and GDEM climatologies, respectively.

Region	**Depth (m)**	**T_0=27.5°C**		**T_0=28.0°C**		**T_0=28.5°C**	
		WOD01	**GDEM**	**WOD01**	**GDEM**	**WOD01**	**GDEM**
ENP (Apr-Jun)	MLD	21.7	22.3	21.6	22.4	21.0	22.1
	Z_T	28.1	27.1	24.1	22.9	18.3	18.1
GoM (Jul-Sep)	MLD	19.9	20.9	20.0	21.0	20.1	21.5
	Z_T	31.2	29.5	27.0	24.5	21.4	18.5
CBN (Aug-Oct)	MLD	41.3	44.1	41.8	44.9	42.4	45.7
	Z_T	54.7	55.2	44.2	43.7	33.4	30.8
EQA (Mar-May)	MLD	31.1	31.9	29.4	29.6	22.2	22.2
	Z_T	33.5	32.1	24.9	24.2	17.2	17.8

Table 3. Q_{NET} from seven heat flux climatologies, averaged within warm pool boundaries (WOD01 isotherms used) for the subregions, as in Table 2 and for the same seasons. The last rows are totals for the entire warm pool and year. Columns are ranked from left to right according to the average amount of heat absorbed by the ocean annually in the Western Hemisphere tropics (30°S-30°N, Africa to 120°W).

Region	T_0	SHU	DSU	OBH	DSC	SHC	NCEP	ERA15
ENP (Apr-Jun)	28.5	85.4	86.3	49.7	49.6	48.0	50.8	22.1
	28.0	81.9	81.6	47.2	46.1	43.3	50.2	18.6
	27.5	79.3	78.6	45.4	43.4	40.4	49.7	17.9
GoM (Jul-Sep)	28.5	91.0	84.4	43.7	42.9	51.2	28.6	-15.0
	28.0	90.8	84.4	43.7	43.0	45.1	29.0	-14.7
	27.5	90.7	84.5	43.7	43.0	42.0	29.0	-14.7
CBN (Aug-Oct)	28.5	73.7	69.0	23.8	29.0	6.6	6.8	-21.7
	28.0	73.2	70.0	22.8	30.0	12.9	-0.2	-19.7
	27.5	73.7	70.6	23.2	30.8	13.7	-0.01	-18.7
EQA (Mar-May)	28.5	80.3	85.8	59.3	49.9	40.2	41.5	1.9
	28.0	81.5	86.7	53.0	50.5	43.0	41.1	-5.6
	27.5	81.9	85.2	50.1	48.8	44.0	40.6	-6.1
TOTAL (Jan-Dec)	28.5	90.7	95.6	65.4	58.9	51.7	49.8	16.0
	28.0	85.4	90.0	56.7	53.1	46.4	44.6	5.9
	27.5	82.9	86.0	51.2	48.6	43.8	39.8	2.0

Table 4. Upper tier: Three-month means of the shortwave radiative flux Q_{SWP} (W/m^2) penetrating past 25 m. Each column applies the attenuation coefficient appropriate for a Jerlov water type (constant in space and time) or for a SeaWiFS-derived satellite algorithm (spatially and temporally variable). All calculations are applied to the DSU incoming shortwave radiative flux at each grid point, then averaged over the indicated subregion (Figure 1) and three-month period. Lower tier: As above, but for the area-averaged 28.0°C isotherm depth (Table 2) within the same subregions and periods. As defined by Jerlov, type I water is the clearest, consistent with subtropical open ocean ("blue") environments, while type III water is most turbid, typical of river outflows and highly productive coastal waters. The subtype IA is closest to but slightly more turbid than type I, while the Jerlov subtype IB is closest to but slightly less turbid than type II.

Z = 25m (fixed) **Jerlov water types** **SeaWiFS algorithms**

Region	I	II	III	MOR	K490	OHL
ENP (APR-JUN)	34.28	26.35	18.35	21.36	23.40	18.07
GoM (JUL-SEP)	37.78	29.04	20.23	20.27	23.95	18.17
CBN (AUG-OCT)	34.15	26.25	18.28	17.89	20.96	15.82
EQA (MAR-MAY)	32.84	25.24	17.58	21.94	26.20	20.34

Z for 28.0°C **Jerlov water types** **SeaWiFS algorithms**

Region	I	II	III	MOR	K490	OHL
ENP (APR-JUN)	38.15	30.92	23.62	26.78	27.68	24.48
GoM (JUL-SEP)	34.32	26.45	18.57	20.24	23.62	17.8
CBN (AUG-OCT)	20.14	15.15	10.51	11.94	14.49	10.51
EQA (MAR-MAY)	36.51	29.36	22.16	26.55	29.9	26.48

Table 5. WHWP bubble analysis heat budget residuals (Q_{DIF}, W/m^2), shown for the WOD01 (upper tier) and GDEM (lower tier) hydrothermal climatologies and for all three defining isotherms. The results are grouped by the three-month periods and basins within which each of the four subregions is at maximum development. Columns are ranked from left to right according to the average amount of heat absorbed by the ocean annually in the Western Hemisphere tropics (30°S-30°N, Africa to 120°W).

Region	T_o	SHU	DSU	OBH	DSC	SHC	NCEP	ERA15
ENP (Apr-Jun)	28.5	-48.7	-48.0	-18.7	-9.6	-15.1	-17.1	6.1
	28.0	-54.4	-52.1	-23.9	-13.8	-20.3	-25.3	4.1
	27.5	-54.5	-51.6	-23.3	-13.5	-20.2	-27.3	2.5
GOM (Jul-Sep)	28.5	-56.6	-51.2	-12.5	-10.4	-19.7	7.7	36.2
	28.0	-53.2	-50.4	-8.1	-9.8	-16.2	15.1	38.5
	27.5	-50.6	-50.6	-7.6	-10.4	-13.4	13.9	38.6
CBN (Aug-Oct)	28.5	-42.0	-34.0	-0.5	5.4	-5.3	19.0	54.3
	28.0	-45.6	-41.5	-6.1	-2.4	-8.8	15.9	51.0
	27.5	-46.9	-45.0	-8.5	-6.1	-9.7	11.4	49.4
EQA (Mar-May)	28.5	-42.7	-48.0	-26.1	-12.3	-10.0	-9.4	25.6
	28.0	-48.1	-52.8	-23.7	-16.4	-14.0	-10.8	30.5
	27.5	-53.5	-56.7	-23.9	-19.7	-18.0	-11.6	30.4

Region	T_o	SHU	DSU	OBH	DSC	SHC	NCEP	ERA15
ENP (Apr-Jun)	28.5	-45.9	-45.5	-16.3	-8.0	-12.9	-14.7	6.3
	28.0	-49.1	-46.9	-18.6	-9.3	-15.6	-19.5	5.3
	27.5	-48.9	-46.1	-18.0	-8.5	-15.1	-21.0	3.6
GOM (Jul-Sep)	28.5	-56.2	-50.5	-14.2	-11.9	-21.4	2.9	29.6
	28.0	-53.4	-50.4	-9.1	-11.6	-17.9	13.2	29.9
	27.5	-53.8	-53.2	-11.0	-14.5	-17.9	8.6	29.5
CBN (Aug-Oct)	28.5	-41.3	-32.0	-0.9	5.4	-6.8	13.8	49.5
	28.0	-46.8	-41.4	-6.5	-3.6	-11.1	15.5	44.7
	27.5	-48.9	-46.0	-10.2	-8.5	-13.1	8.7	42.0
EQA (Mar-May)	28.5	-49.2	-53.6	-30.7	-18.9	-17.4	-12.9	18.4
	28.0	-49.1	-54.2	-25.3	-18.9	-15.8	-12.5	26.6
	27.5	-53.0	-56.4	-23.9	-20.4	-18.7	-12.7	25.7

Table 6. Rows summarize the slab heat balance for the four subregions and their respective seasons of maximum development, using the bubble residuals for the 28.0°C and 27.5°C isotherms (Table 4) as estimates for the total diffusive heat flux (equation 2, term *D*). Columns from left to right are the bounding temperature (°C), the WOD01 storage rate, the net heating from five surface flux climatologies; and the corresponding residuals taken as estimates of the total advective heat flux divergence. Units are in W/m^2.

AREA	T_o	dH/dt	$Q_{NET} - Q_{SWP}$			Q_{DIF}			Q_{RES}		
		WOD01	OBH	DSC	SHC	OBH	DSC	SHC	OBH	DSC	SHC
ENP (Apr-Jun)	28.0	-0.4	24.6	13.5	19.0	-23.9	-13.8	-20.3	-1.1	-0.1	0.9
	27.5	0.0	28.3	18.0	23.1	-23.3	-13.4	-20.2	-5.0	-4.6	-2.9
GOM (Jul-Sep)	28.0	2.2	24.9	19.3	29.0	-8.1	-9.8	-16.2	-14.6	-7.3	-10.6
	27.5	4.7	27.9	23.1	32.5	-7.6	-10.4	-13.4	-15.6	-8	-14.4
CBN (Aug-Oct)	28.0	8.1	14.6	20.4	25.2	-6.1	-2.4	-8.8	-0.4	-9.9	-8.3
	27.5	10.7	17.4	24.0	28.5	-8.5	-6.1	-9.7	1.8	-7.2	-8.1
EQA (Mar-May)	28.0	-5.5	26.5	21.5	21.0	-23.7	-16.4	-14.0	-8.3	-10.6	-12.5
	27.5	-6.9	33.3	29.8	28.8	-23.9	-19.7	-18.0	-16.3	-17.0	-17.7

Table 7. Rows summarize of the overall heat balance for the four subregions and their respective seasons of maximum development, using only the three optimal surface flux climatologies (DSC, SHC, OBH) and the corresponding diffusion estimates averaged for the 28.0°C and 27.5°C isotherms. Columns from left to right are the WOD01 storage rate, the net heating from Table 5; the bubble residual estimate of Q_{DIF} from Table 4; and the slab residual estimate of the total advective heat flux divergence. Each of the flux columns is a range separated by dotted vertical lines based on the surface fluxes. The column on the far right gives the range of total advective heat flux divergence directly estimated from drifter observations and the da Silva and Southampton wind stress climatologies. Units in W/m^2.

Region	***dH/dt* (WOD01)**	Q_{NET}-Q_{SWP}		Q_{DIF}		Q_{RES}		Q_{ADV}	
ENP (Apr-Jun)	-0.2	26.5	15.8	-23.6	-13.6	-3.3	-1.3	-2.0	-2.0
GoM (Jul-Sep)	3.5	30.8	21.2	-14.7	-7.9	-15.1	-7.6	-5.5	-5.4
CBN (Aug-Oct)	9.4	26.9	16.0	-9.3	-4.3	-8.5	0.7	- -	- -
EQA (Mar-May)	-6.2	29.9	24.9	-23.8	-16.0	-15.1	-12.3	- -	- -

Figure captions

Figure 1. Subregions of the Western Hemisphere warm pool analyzed in this study: eastern North Pacific (ENP); Gulf of Mexico (GoM); Caribbean (CBN) and the equatorial Atlantic (EQA).

Figure 2. Distribution of the 27.5°C, 27.0°C and 28.5°C isotherms (solid contours) from the WOD01 hydrothermal climatology. For comparison the 28.0°C isotherm is shown for the FNOC's GDEM hydrothermal data (dotted contour).

Figure 3. Map comparisons of the 28.0°C isotherm depth against the WOD01 mixed layer depth for the warm pool months of May, July and September.

Figure 4. Map comparisons for the two extremes of the seven surface flux climatologies used in the study: da Silva (unconstrained, left) and ERA15 (ECMWF, middle). The third (right) column of maps shows the difference distribution. Units are W/m^2.

Figure 5. Contour map of the irradiance attenuation depth derived from color satellite (SeaWiFS) imagery by the K490 method (McLain et al. 2002). The Jerlov (1976) optical water types are superimposed (Roman numerals).

Figure 6. Annual variation of the bubble heat balance (constant isotherm boundary) for the eastern north Pacific, using the 27.5°C isotherm. Upper panel: sea surface temperature (°C, solid) and heat storage rate (W/m^2, solid + symbol) from the WOD01 hydrothermal climatology; middle panel: net heating defined as the net surface flux minus the K490-estimated penetrative radiant flux, for seven surface flux climatologies (W/m^2, legend at bottom); and bottom panel: residual estimates of the total diffusive flux divergence corresponding to the data sets used in the middle panel (W/m^2).

Figures 7. For the eastern North Pacific as in Figure 6, but using the 28.5°C isotherm instead of 27.5 °C.

Figures 8. Using the 27.5°C isotherm as in Figure 6, but for the Atlantic.

Figures 9. For the Atlantic as in Figure 8, but using the 28.5°C isotherm instead of 27.5 °C.

Figure 10. Annual variation of surface forcing terms for the constant isotherm region (bubble) in the eastern North Pacific, using the 27.5°C isotherm. Upper panel: sea surface temperature (°C, solid) and heat storage rate (W/m^2, solid + symbol) from the Levitus hydrothermal climatology; middle panel: heat flux terms with large seasonal cycles from the constrained Southampton surface heat flux climatology (SHC), namely shortwave radiative flux (Q_{SWR}), latent heat flux (Q_{EVP}), penetrative shortwave flux (Q_{SWP}) and also the net surface heating (Q_{NET}), all with their annual means removed; and bottom panel: the net shortwave radiative flux at the sea surface (Q_{SWR}), downward shortwave radiative flux at the top of the atmosphere (Q_{TOA}), with their annual means removed in both, and the cloud fraction.

Figures 11. As in Figure 10, but for the Atlantic portion of the WHWP.

Figures 12. Vector estimates of annual average horizontal flow (m/s) from surface drifters with 15 m drogues. Data have been binned into the boxes shown with 1/4° latitude cross-channel width and 6° latitude length in the through-channel direction. For the bin closest to Yucatan (no data) the flow is interpolated between the coast (zero) and the next bin to the east.

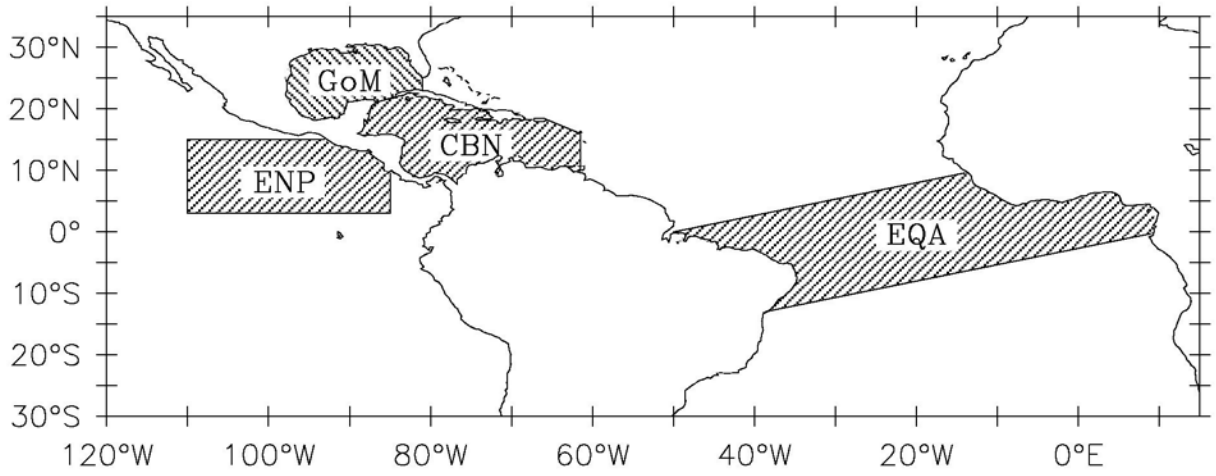
30°N
20°N
10°N
0°
10°S
20°S
30°S
120°W
100°W
80°W
60°W
40°W
20°W
0°E
GoM
CBN
ENP
EQA

Figure 1

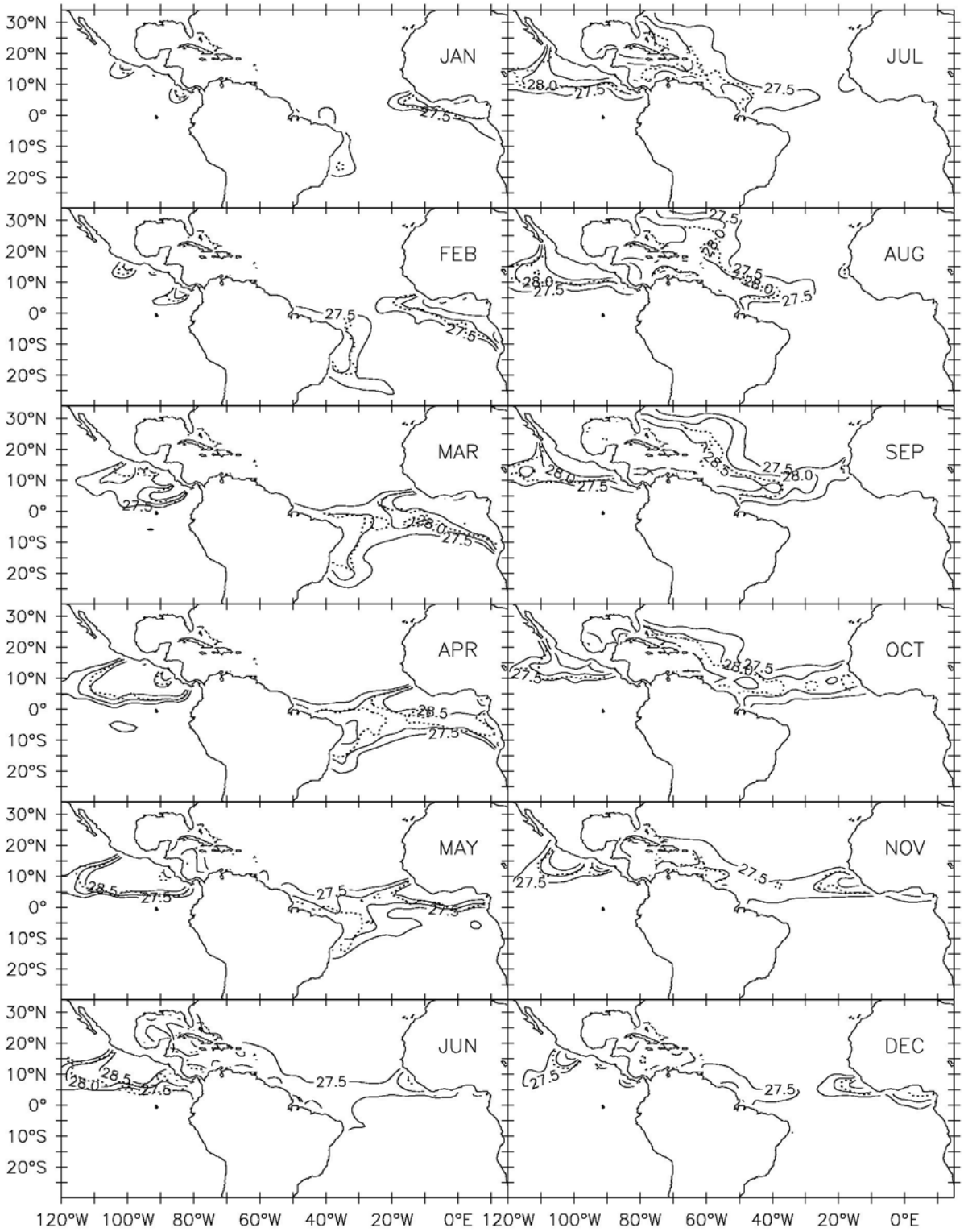
JAN
JUL
FEB
AUG
MAR
SEP
APR
OCT
MAY
NOV
JUN
DEC
30°N
20°N
10°N
0°
10°S
20°S
120°W
100°W
80°W
60°W
40°W
20°W
0°E
27.5
28.0
28.5

Figure 2

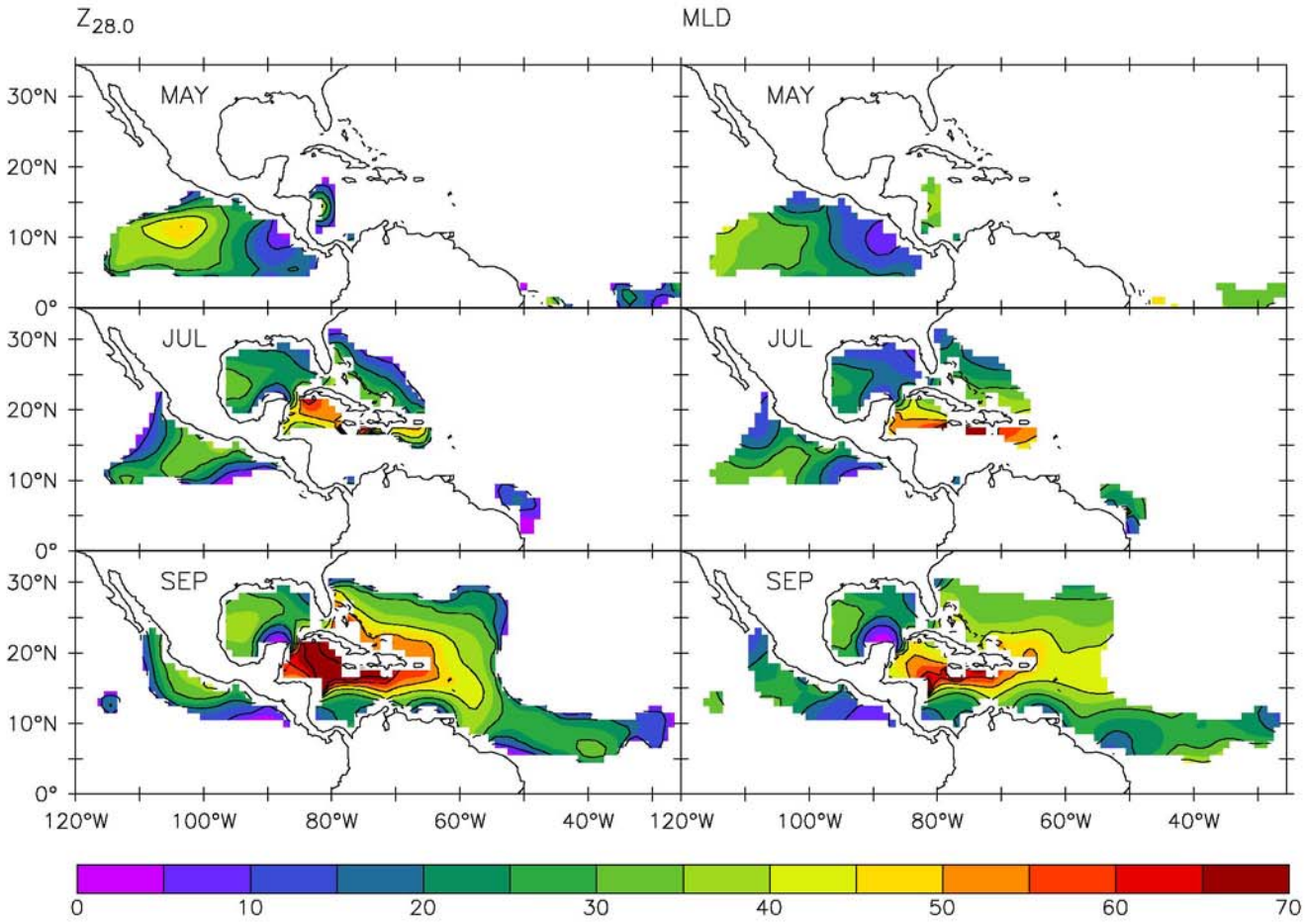
$Z_{28.0}$
MLD
MAY
MAY
JUL
JUL
SEP
SEP
30°N
20°N
10°N
0°
120°W
100°W
80°W
60°W
40°W
0
10
20
30
40
50
60
70

Figure 3

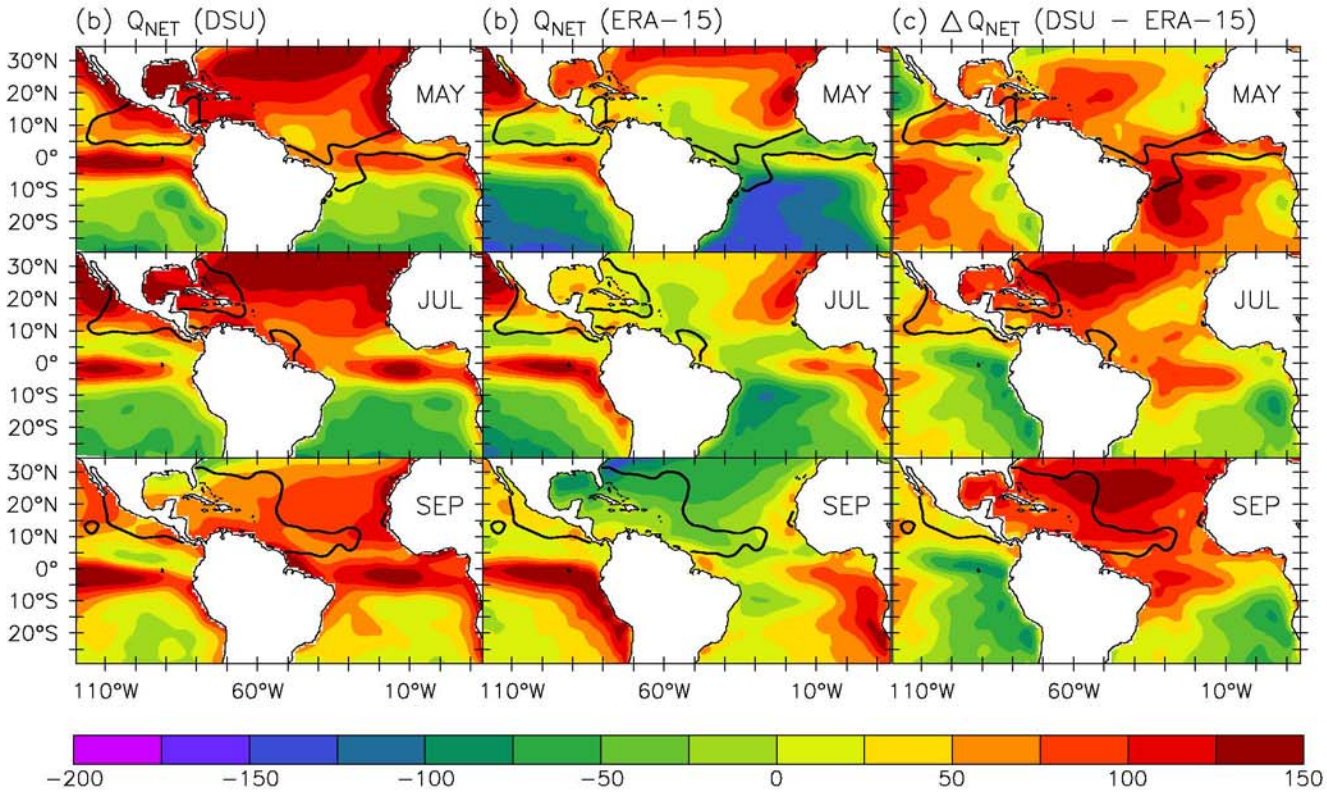
(b) Q_{NET} (DSU)
(b) Q_{NET} (ERA−15)
(c) ΔQ_{NET} (DSU − ERA−15)
MAY
JUL
SEP
30°N
20°N
10°N
0°
10°S
20°S
110°W
60°W
10°W
−200
−150
−100
−50
0
50
100
150

Figure 4

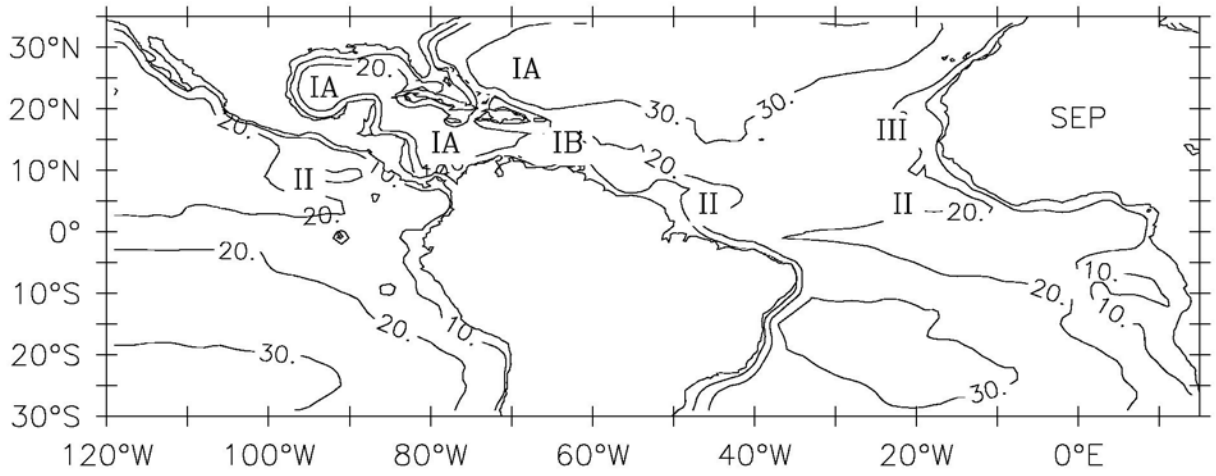
30°N
20°N
10°N
0°
10°S
20°S
30°S
120°W
100°W
80°W
60°W
40°W
20°W
0°E
IA
IA
IA
IB
II
II
II
III
SEP
20.
30.
10.

Figure 5

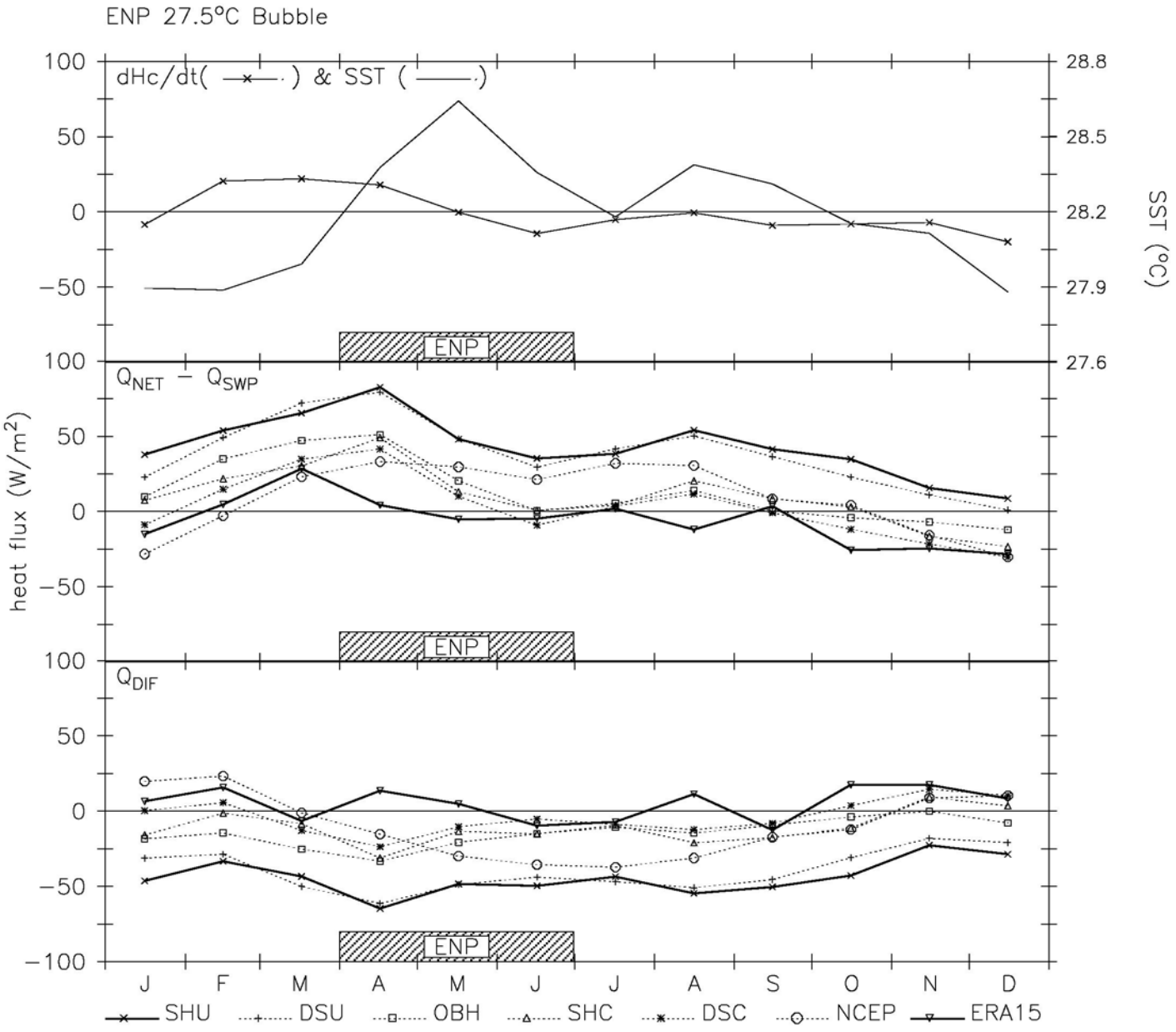
ENP 27.5°C Bubble
dHc/dt( ) & SST ( )
SST (°C)
28.8
28.5
28.2
27.9
27.6
ENP
$Q_{NET} - Q_{SWP}$
heat flux (W/m²)
Q_{DIF}
100
50
0
−50
−100
J F M A M J J A S O N D
SHU DSU OBH SHC DSC NCEP ERA15

Figure 6

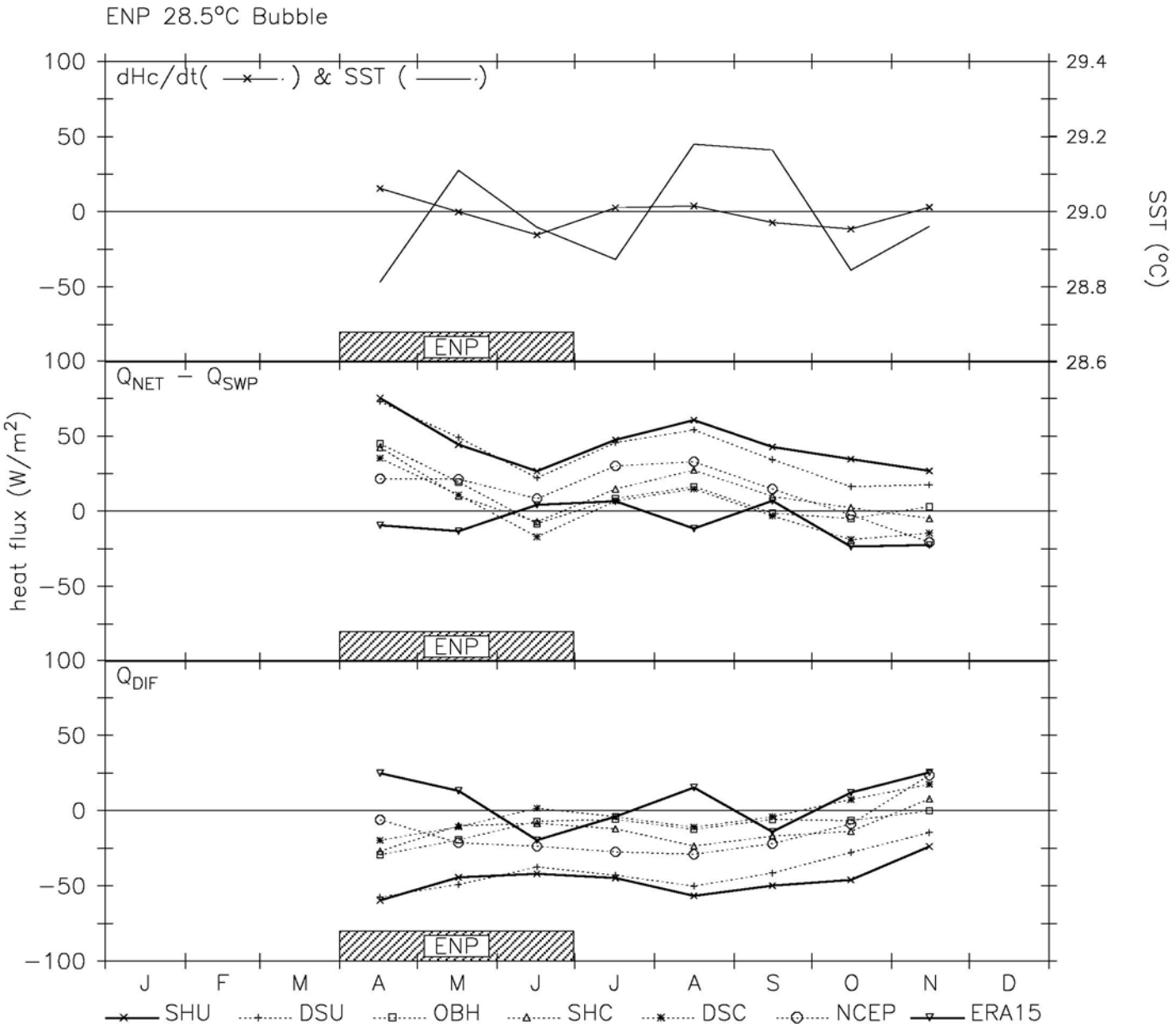
ENP 28.5°C Bubble
dHc/dt( ) & SST ( )
100
50
0
−50
100
29.4
29.2
29.0
28.8
28.6
SST (°C)
ENP
Q_{NET} − Q_{SWP}
heat flux (W/m²)
50
0
−50
100
ENP
Q_{DIF}
50
0
−50
−100
ENP
J F M A M J J A S O N D
SHU DSU OBH SHC DSC NCEP ERA15

Figure 7

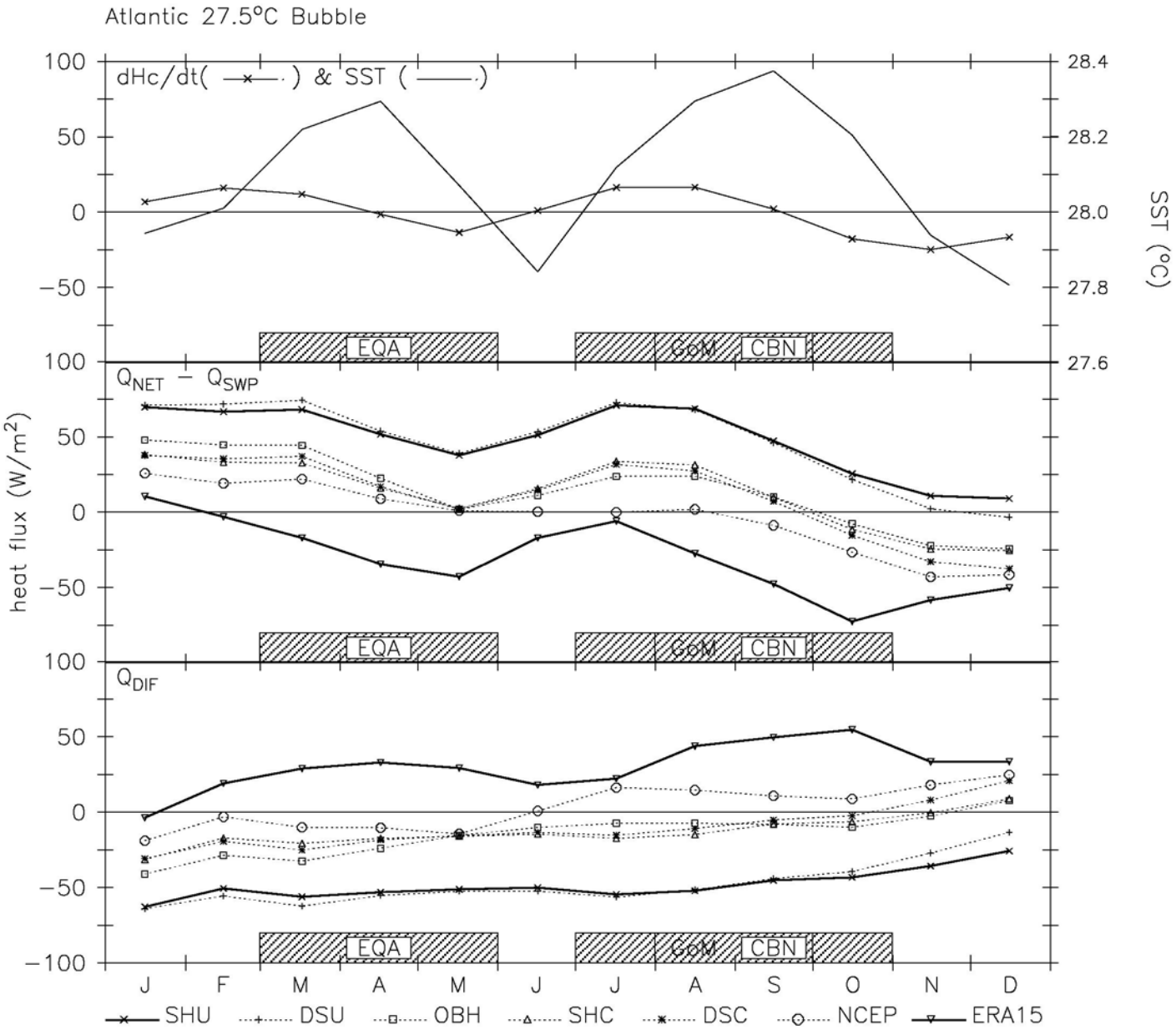
Atlantic 27.5°C Bubble
dHc/dt( ) & SST ( )
SST (°C)
heat flux (W/m²)
Q_NET − Q_SWP
Q_DIF
EQA
GoM
CBN
J F M A M J J A S O N D
SHU DSU OBH SHC DSC NCEP ERA15

Figure 8

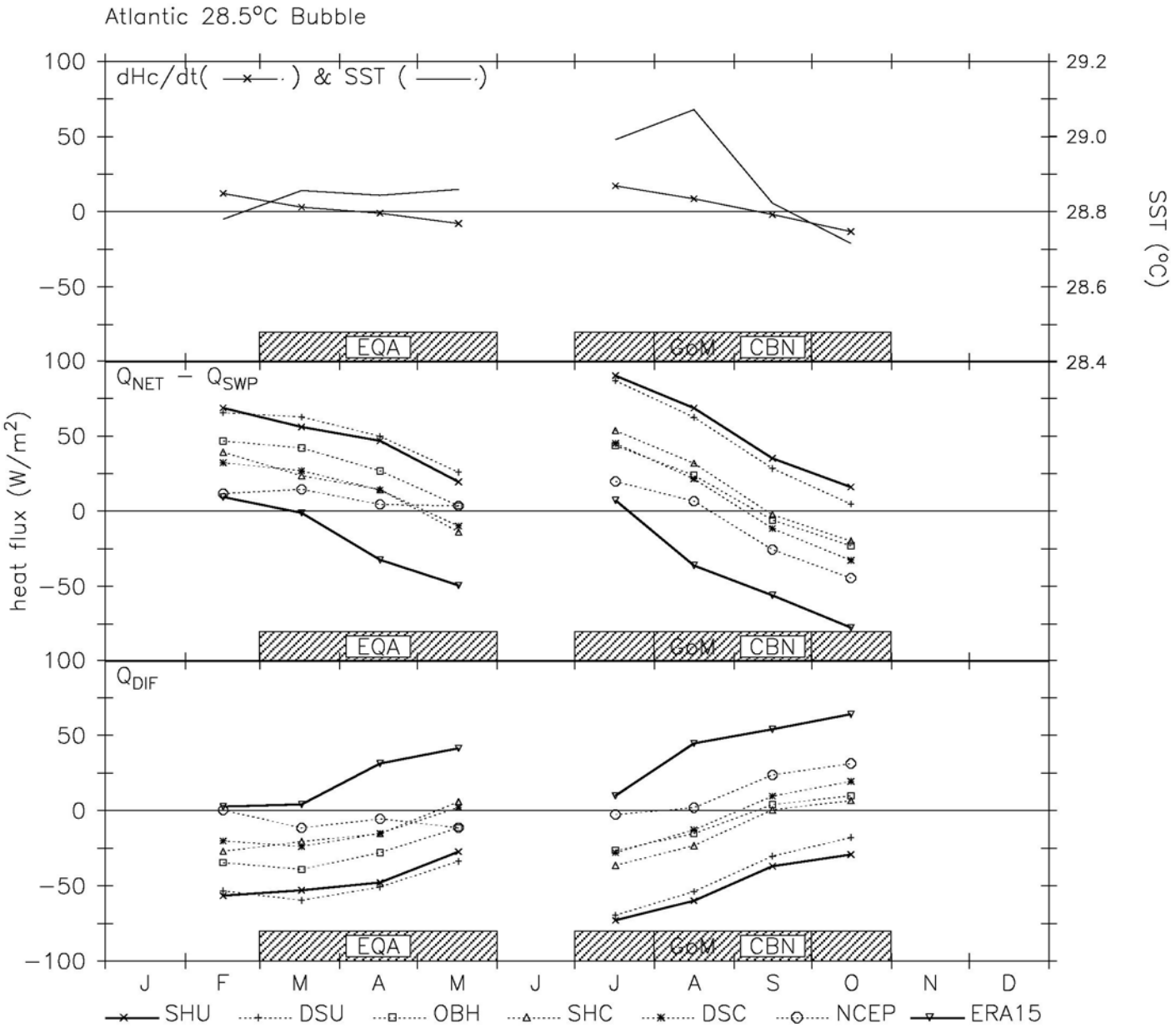
Atlantic 28.5°C Bubble
dHc/dt( ) & SST ( )
100
50
0
−50
29.2
29.0
28.8
28.6
28.4
SST (°C)
EQA
GoM
CBN
Q_{NET} − Q_{SWP}
heat flux (W/m²)
Q_{DIF}
−100
J
F
M
A
M
J
J
A
S
O
N
D
SHU
DSU
OBH
SHC
DSC
NCEP
ERA15

Figure 9

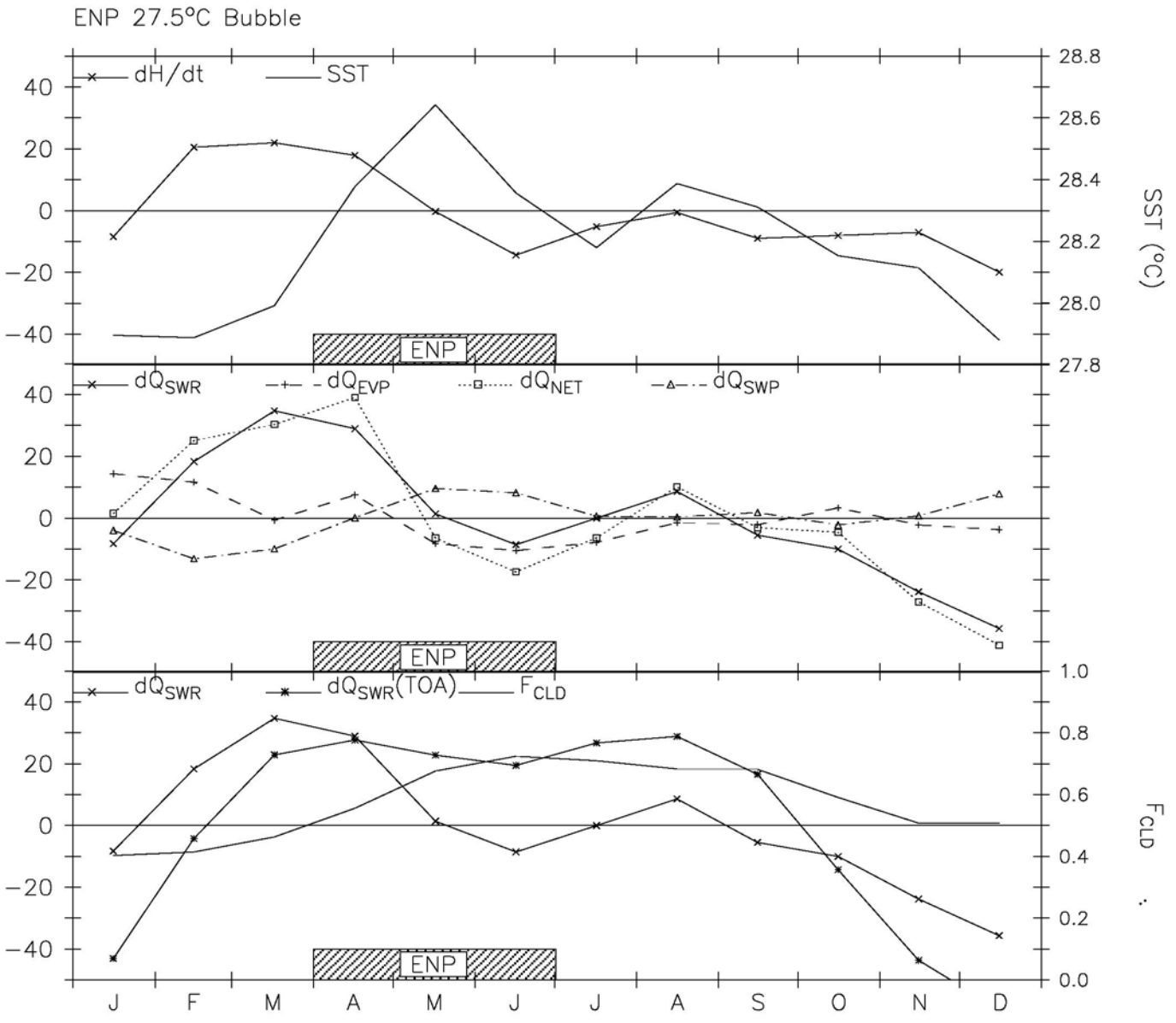
ENP 27.5°C Bubble
dH/dt
SST
ENP
dQSWR
dQEVP
dQNET
dQSWP
ENP
dQSWR
dQSWR(TOA)
FCLD
ENP
40
20
0
−20
−40
28.8
28.6
28.4
28.2
28.0
27.8
SST (°C)
1.0
0.8
0.6
0.4
0.2
0.0
FCLD
J
F
M
A
M
J
J
A
S
O
N
D

Figure 10

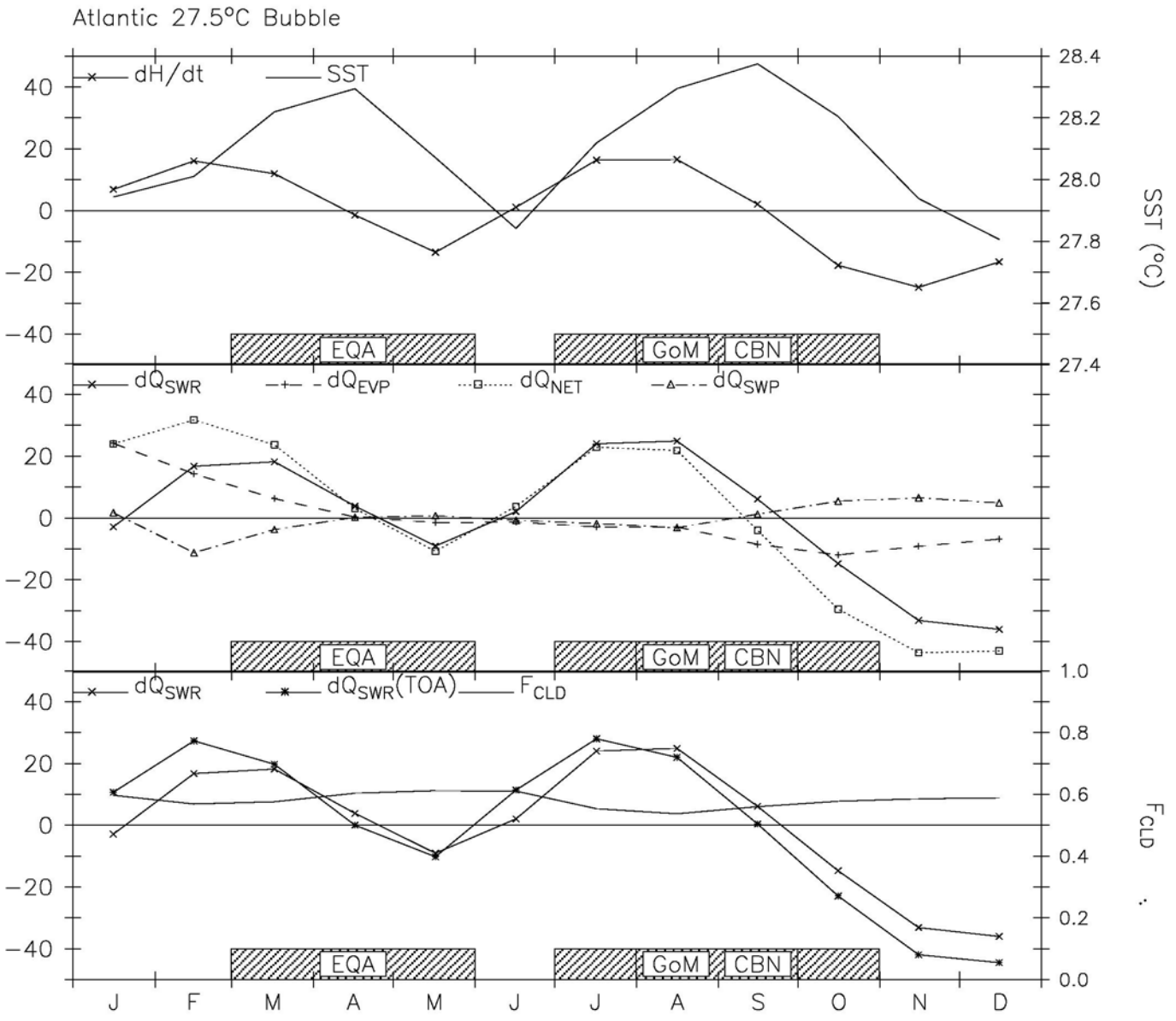
Atlantic 27.5°C Bubble
dH/dt
SST
dQSWR
dQEVP
dQNET
dQSWP
dQSWR
dQSWR(TOA)
FCLD
EQA
GoM
CBN
SST (°C)
FCLD
J
F
M
A
M
J
J
A
S
O
N
D

Figure 11

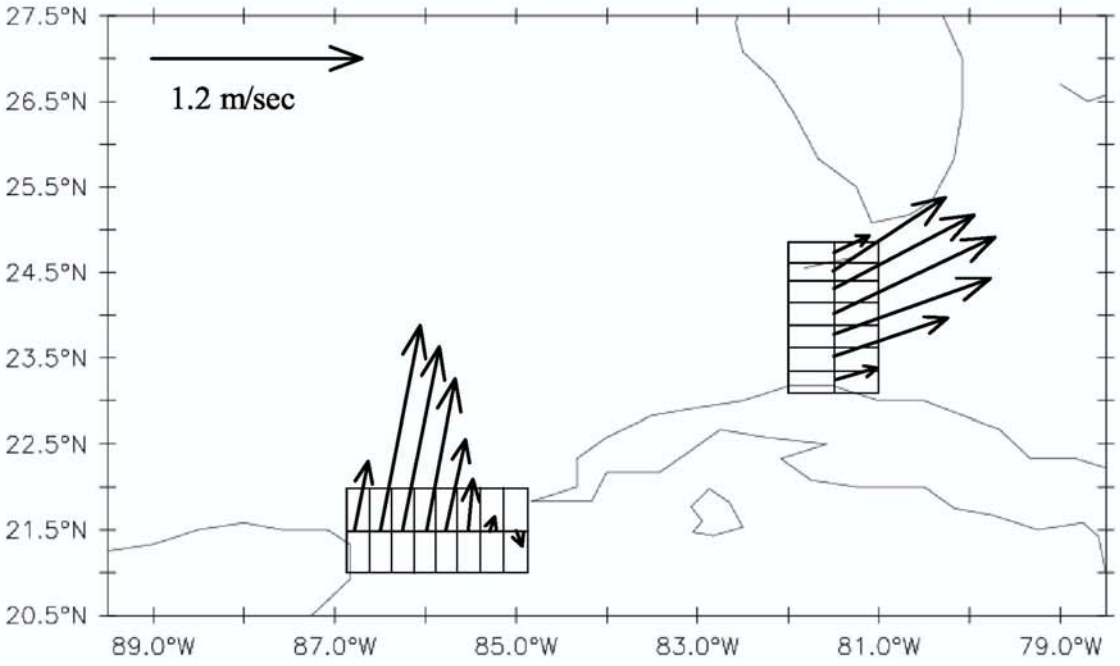
1.2 m/sec
27.5°N
26.5°N
25.5°N
24.5°N
23.5°N
22.5°N
21.5°N
20.5°N
89.0°W
87.0°W
85.0°W
83.0°W
81.0°W
79.0°W

Figure 12